ELSEVIER

High cycle fatigue response of grain refined EUROFER97

Dario Croccolo [a], Andrea Di Schino [b], Roberto Montanari [c], Giorgio Olmi [a,*], Giulia Stornelli [b], Claudio Testani [d], Alessandra Varone [c]

[a] Department of Industrial Engineering (DIN), University of Bologna, Bologna, Italy
[b] Department of Engineering, University of Perugia, 06125 Perugia, Italy
[c] Department of Industrial Engineering, University of Rome Tor Vergata, Rome, Italy
[d] CALEF-ENEA CR-Casaccia, S. Maria di Galeria, Rome, Italy

ARTICLE INFO

ABSTRACT

The present paper has investigated the high cycle fatigue behavior of EUROFER97 steel submitted to a novel process consisting of cold rolling with reduction ratio of 80 % followed by a heat treatment at 650 °C for 1 h. This process had already proved to be highly effective under static loads leading to a significant improvement in yield stress. The fatigue tests have been performed with 0.2 load ratio at room temperature. Results indicate that the fatigue strength of the steel submitted to the novel treatment is comparable to that of the standard EUROFER97. Moreover, the fatigued samples underwent a microstructural evolution consisting of grain size increase and texture change due to the stress-driven instability of grain boundaries, especially LAGBs. The collapse of some boundaries involves partial annihilation and re-arrangement of dislocations, and grain coalescence. As a consequence of such microstructural change the material softens with hardness variations up to 8 %.

1. Introduction

EUROFER97 is the reference steel for manufacturing structural components of the test blanket module of the International Thermonuclear Experimental Reactor (ITER) [1–3] and a promising candidate material for the first wall and other highly stressed sections as blanket, vessel, and divertor in Demonstration Power Plant (DEMO) [4–7]. This reduced activation ferritic-martensitic steel exhibits good weldability [8] and excellent mechanical properties also at high temperature [9]. After neutron irradiation [9,10] and He ion implantation [11,12] EUROFER97 has good mechanical performances between 350 and 550 °C, and several studies have been carried out to extend this operating temperature range. To raise the upper limit to about 600–650 °C, a possible solution is to reinforce the steel through yttrium oxides (Y_2O_3) of nanometric size, which inhibit grain boundary sliding and retard grain growth at high temperature [13,14]. Oxide dispersion-strengthened steel (ODS-EUROFER97) is commonly produced by mechanical alloying, and hot extrusion followed by a heat treatment at high temperature (1100 °C).

The lower temperature limit (350 °C) is mainly connected to the ductility loss induced by defects produced by neutron irradiation [15]. In general, grains of lower size increase strength and promote better

irradiation strength and reduced He/H susceptibility because grain boundaries act as sinks for Frenkel pairs produced by irradiation and traps for He and H atoms [16,17]. However, grain refinement often involves a loss of ductility at low temperature due to the increased dislocation density.

EUROFER97 is heat treated through a standard process consisting of: austenitization at 980 °C for 30 min, air cooling to room temperature, tempering at 760 °C for 90 min and final air cooling to room temperature. The resulting microstructure is a tempered lath martensite.

Recently, an extended experimental campaign has been carried out by us for developing a thermo-mechanical process suitable to improve mechanical strength without reducing ductility [18,19]. The idea was to achieve a population of fine grains with low dislocation density through cold rolling and successive recrystallization. Therefore, EUROFER97 in standard condition has been submitted to 40 different thermo-mechanical treatments by combining five cold rolling reduction (CR) ratios (20, 40, 50, 60 and 80 %) and eight heat treatments at temperatures from 400 °C to 750 °C with steps of 50 °C (soaking time of 1 h) and the best combination of mechanical properties was obtained by a reduction ratio of 80 % followed by a treatment at 650 °C. As shown by Table 1, the novel treatment improves hardness, Yield Stress (YS) and Ultimate Tensile Strength (UTS) with the same total elongation A% of

Table 1

Mechanical properties at room temperature of EUROFER97 produced through the standard and novel treatment.

Treatment	Hardness HV$_5$	Yield stress [MPa]	Ultimate tensile strength [MPa]	A%
Standard	206 [20]	550 [21]	657 [21]	22 [22]
Novel	235 [19]	650 [19]	690 [19]	22 [19]

Table 2

Nominal chemical composition of EUROFER97 steel (wt.%) (Fe to balance) [29].

Cr	C	Mn	V	W	Ta	Ti	N
8.93	0.12	0.47	0.2	1.07	0.14	0.009	0.018
P	**S**	**B**	**Si**	**Nb**	**Mo**	**Ni**	**Cu**
<0.005	0.004	<0.001	0.006	0.002	0.0015	0.002	0.003

standard EUROFER97.

Low cycle fatigue (LCF) of standard EUROFER97 has been investigated at temperature up to 550 °C [23,24], also assessing the effect of different load cycles. The reported experimental results at room temperature, interpolated by the Manson-Coffin model, indicate that a strain amplitude of 0.2 %, mainly consisting of elastic strain (along with a negligible plastic residual), results in an observed life of about 5×10^4 cycles. Moreover, it has been found that, from room temperature to 550 °C, the influence of the test temperature on the fatigue endurance is not significant [23]. Walter et al. [25] performed LCF tests by changing the total strain amplitude during a single experiment and EUROFER97 response has been assessed when high amplitude cyclic loads precede the low amplitude ones or vice versa. The results indicate a not linear damage accumulation and that higher initial loads result in shorter life.

Multiaxial fatigue tests with superimposed tension and torsion at room and increased temperature have been carried out by Weick and Aktaa [26]. The results revealed the influence of the phase shift for different temperatures as well as the influence of the test execution method (fixed or rotating principal stress system).

Petersen et al. [27] investigated the effect of irradiation (fast neutron flux of $1.8 \times 10^{15} n/cm^2 s$, direct Na cooling at a temperature <340 °C, 15 and 30 dpa) evidencing that LCF shows at total strains below 1 % an increase of number of cycles to failure, due to irradiation hardening. LCF tests [28], performed at 300 °C in the unirradiated and irradiated conditions, highlighted the beneficial or detrimental effects of irradiation under low and high strain ranges, respectively. The given explanation is that at low strain the fatigue damage is postponed by the strong pinning obstacles induced by irradiation whereas at high strain it grows faster due to localization of deformation.

This work aims to investigate the fatigue behavior of EUROFER97 after the novel process in comparison to the standard one. Fatigue tests have been run in the high cycle regime and at room temperature. The results have been interpolated via linear, non-linear and probabilistic models and discussed by considering the metallurgical characteristics of the material and metallographic analyses of fractured surfaces. Points of innovation arise from the total absence of previous studies addressing the fatigue response of EUROFER97 under the aforementioned novel thermo-mechanical treatment.

2. Materials and methods

2.1. Material processing and fatigue probes

The nominal chemical composition of the examined EUROFER97 steel (batch 2) is reported in Table 2.

A plate of EUROFER97 steel in standard condition was cold rolled with a reduction ratio of 80 %. Afterward, according to the drawing in Fig. 1, flat samples for fatigue tests have been cut by electrical discharge machining (EDM).

Each sample has been heat-treated at 650 °C for 1 h in argon atmosphere and checked by light microscopy observations (LM-Union Optical Co., Ltd., Tokyo, Japan) to exclude the presence of significant defects that may have detrimental effects on fatigue testing results. As a final step before testing, all the samples have undergone dimensional and roughness (RT-25, by Alpa Metrology, Brescia, Italy) checks. Since EDM cutting may introduce slight deviations from the nominal dimensions, each sample was accurately measured to properly correlate the applied load to the resulting stress during fatigue testing. The
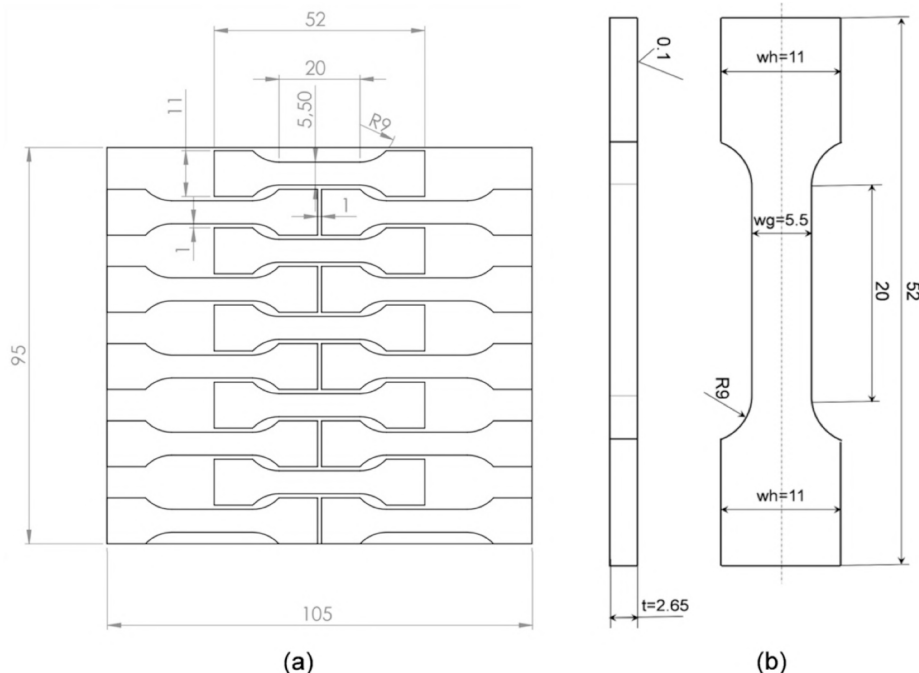

Fig. 1. Sample cutting from the cold rolled sheet (a); sample drawing with dimensions in mm (b).

standard deviations were generally lower than 0.036 mm. Roughness has been measured at the gage on both sides of each sample for a total of six measurements. The average value Ra = 0.027 ± 0.006 μm is consistent with that recommended by many standards dealing with fa-

[32–37]. This is made possible by the monotonic trend of the logarithm function and by its property of converting products into sums, which results in a better computational efficiency and accuracy.

$$L = \prod_{i=1}^{n} \left\{ \phi\left(\frac{Log(N_i) - (b_0 + b_1 \bullet Log(S_i))}{\sigma_{Log(N)}}\right)^{\delta_i} \Phi\left(\frac{S_i - \mu_S}{\sigma_S}\right)^{\delta_i} \left[1 - \Phi\left(\frac{Log(N_i) - (b_0 + b_1 \bullet Log(S_i))}{\sigma_{Log(N)}}\right) \Phi\left(\frac{S_i - \mu_S}{\sigma_S}\right)\right]^{1-\delta_i} \right\} \quad (3)$$

$$ln(L) = \sum_{i=1}^{n} ln\left\{ \phi\left(\frac{Log(N_i) - (b_0 + b_1 \bullet Log(S_i))}{\sigma_{Log(N)}}\right)^{\delta_i} \Phi\left(\frac{S_i - \mu_S}{\sigma_S}\right)^{\delta_i} \left[1 - \Phi\left(\frac{Log(N_i) - (b_0 + b_1 \bullet Log(S_i))}{\sigma_{Log(N)}}\right) \Phi\left(\frac{S_i - \mu_S}{\sigma_S}\right)\right]^{1-\delta_i} \right\} \quad (4)$$

tigue testing (e.g. see ref. [30]).

2.2. Fatigue tests

The fatigue trials have been performed by a resonant machine (20 kN capacity, by Rumul Switzerland) under tension–tension with a stress ratio R = 0.2 and at the frequency f = 113 Hz. This machine operates under load control and, based on the actual cross-section area of each sample, the load pattern to be applied has been determined and controlled to generate the desired stress cycle. The experimental set-up used for fatigue tests (a) and a detail of sample mounting (b) are shown in Fig. 2. The failure criterion was crack initiation. Crack onset results in specimen axial stiffness abrupt drop that, in turn, entails significant reduction of natural frequency (and actual testing frequency), which triggers resonant machine stop. The reported lifecycles to failure refer to this condition. The complete separation of samples into two pieces has been then achieved through the application of a static load. A run-out value of 10^7 cycles has been set, based on previous results under LCF [23,24].

2.3. Analytical treatment of data from fatigue tests

The S-N curve has been processed by two methods: by International Standards and by a "Maximum Likelihood Estimation (MLE)" approach. Regarding the first methodology, the interpolation of data has been described in detail in ref. [31]. In particular, both the linear (Eq. (1)) and the quadratic (Eq. (2)) models have initially been used:

$$Log(N) = b_0 + b_1 \bullet Log(S) \quad (1)$$

$$Log(N) = b_0 + b_1 \bullet Log(S) + b_2 \bullet Log^2(S) \quad (2)$$

where N and S are lifecycles and maximum stress at gage, respectively, while b_0, b_1 and b_2 are interpolation constants.

Finally, the General Linear Test has been applied to determine if the improvement yielded by the more sophisticated quadratic model was significant. The analysis has been completed by the determination of confidence bounds for 10 and 90 % probabilities of failure and 90 % confidence level. A possible limitation of this conventional approach is that failure data only can be considered for interpolations. Therefore, an MLE approach has also been applied. This procedure allowed to work out stress-lifecycles curves, accounting for both failure data, tagged as complete or "not censored" and run-outs, commonly regarded as "censored" or "censoring" data. The application of this method entails the proper determination of both the S-N curve in the finite life domain (for high-stress levels) and the fatigue limit for infinite life. The curvature at the transition between the sloping part and the constant trend corresponding to the fatigue limit is also suitably modelled. This method, previously applied by Croccolo et al. [32], is based on the maximization of the likelihood function L, expressed by Eq. (3). The maximization procedure is usually made in logarithmic scale (see Eq. (4)

In Eqs. (3) and (4) N_i are the observed lives for tests with R = 0.2 under the maximum stress S_i. It is supposed that the 10-base logarithm of the fatigue life is normally distributed with standard deviation $\sigma_{Log(N)}$, and that the fatigue limit is normally distributed with mean value μ_S and standard deviation σ_S. Φ indicates the cumulative distribution function of the Normal distribution, ϕ is the probability density function of the same distribution, δ_i assumes the values 1 or 0 for failure (complete) and run-out (censoring) data, respectively, and n is the overall number of tests, including both failure and run-out events.

First, the fatigue curve for a probability of failure of 50 % has been determined. Subsequently, lower and upper bounds corresponding to failure probabilities of respectively 10 % and 90 % have been determined as well. For these purposes, the relationship in Eq. (5) has been inverted to work out the predicted life $\overline{N}$ for a (maximum) stress $\overline{S}$, considering a probability of failure p.

$$p = \Phi\left(\frac{Log(\overline{N}) - (b_0 + b_1 \bullet Log(\overline{S}))}{\sigma_{Log(N)}}\right) \cdot \Phi\left(\frac{\overline{S} - \mu_S}{\sigma_S}\right) \quad (5)$$

2.4. Microstructural examination

The material before and after fatigue tests has been examined by X-ray diffraction (XRD) in Bragg-Brentano configuration to determine texture, dislocation density ρ and mean size $<D>$ of coherently diffracting domains.

The XRD patterns were collected in step-scanning mode in the 2θ range 15°−60° using the Mo-Kα radiation (λ = 0.070926 nm) with 2θ steps of 0.05° and counting time in steps of 2 s. Preferred grain orientation has been evaluated from the relative peak intensities of the strongest reflections.

Dislocation density and size of crystalline domains were determined from precision peak profiles recorded with 2θ steps of 0.005° and counting time per step of 4 s. Peak profiles were fitted by Lorentzian curves to eliminate the Kα2 component, then the full width at half maximum (FWHM) was corrected from the instrumental broadening. The total broadening β_T is given by the sum of two contributions, β_D and β_ε, due to $<D>$ and micro-strains ε, respectively:

$$\beta_T = \beta_D + \beta_\varepsilon = \frac{0.89\lambda}{<D>\cos\theta} + 2\varepsilon\tan\theta \quad (6)$$

The Cauchy procedure was used to determine $<D>$ and ε, then the dislocation density ρ was calculated through the Williamson-Smallman equation [38]:

$$\rho = \frac{\Xi\varepsilon^2}{Fb^2} \quad (7)$$

being Ξ = 16.1 a constant, $F \approx 1$ a factor depending on the interaction of dislocations and b = 0.248 nm the modulus of Burgers vector.

Electron Back-Scattered Diffraction (EBSD) measurements were performed to determine the texture by means of a field emission gun
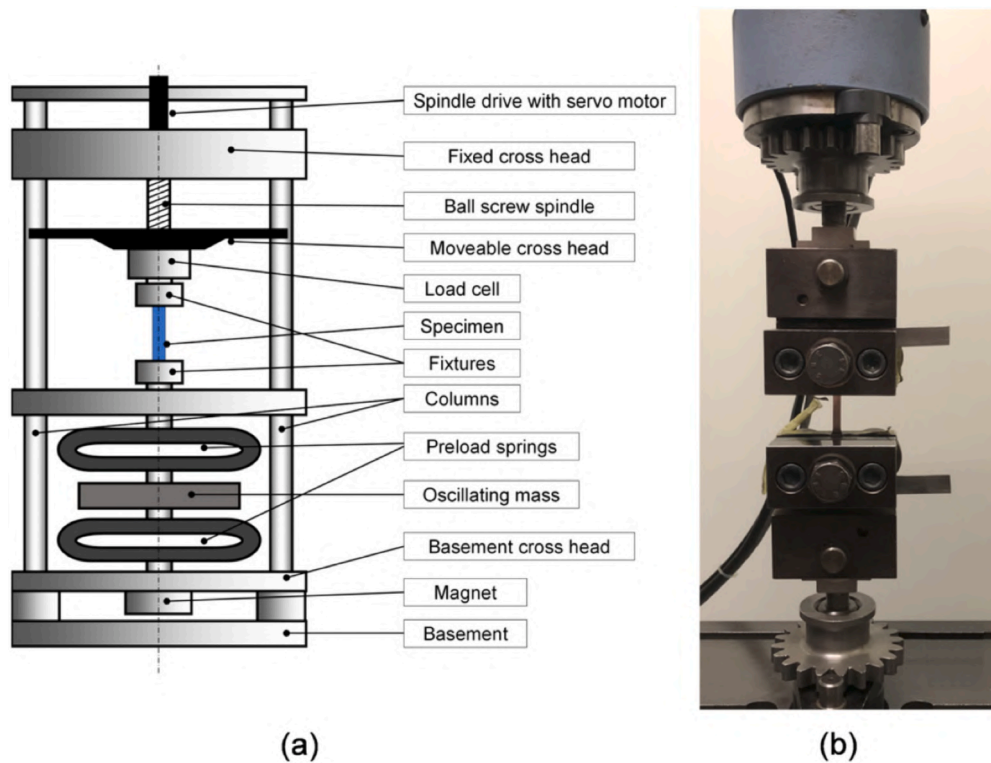
Fig. 2. Experimental set-up used for fatigue tests (a) and detail of sample mounting (b).

scanning electron microscope (FEG-SEM) (Ultra-Plus Carl-Zeiss- Ober-kochen, Germany) equipped with an EBSD detector (C Nano Oxford Instruments, UK) with a step size of 5 μm. The technique was also used to determine the average grain size, the grain size distribution and the typology of grain boundaries.

After fatigue tests the fracture surfaces were investigated by stereo-graphic (SM) and scanning electron microscopy (SEM) observations.

3. Results and discussion

3.1. Microstructural examination of the original material

Fig. 3 displays the XRD pattern of EUROFER97 steel subjected to the novel process consisting of cold rolling with 80 % of reduction ratio
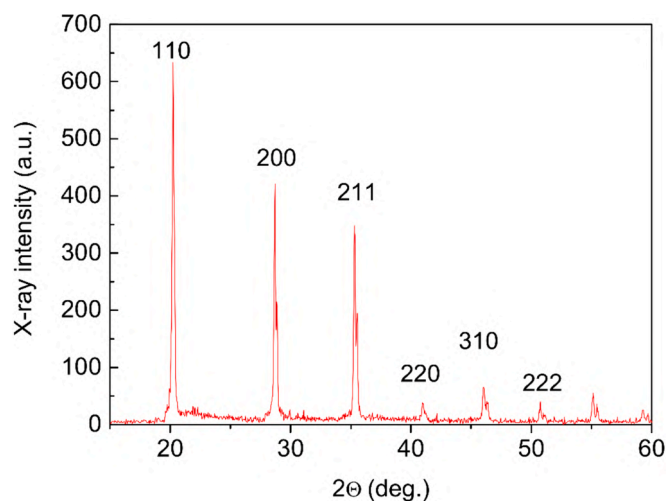

Fig. 3. XRD pattern of EUROFER97 after the novel process (CR:80 %/650 °C for 1 h).

followed by the heat treatment of 1 h at 650 °C.

Table 3 reports the relative intensities of XRD peaks determined from the pattern in Fig. 3. The comparison between these data and those of Fe with randomly oriented grains taken from the JCPDS database (file 6-696) [39] shows that the material has a strong [0 0 1] cubic texture.

From the analysis of high precision peak profiles, the dislocation density $\rho = 10^9$ cm^{-2} and the mean size of coherently diffracting domains $< D > = 210$ nm were determined. The results of EBSD measurements are displayed in Fig. 4: EBSD map (b) collected on the surface of a probe, plane XY (c), inverse polar figures (d), grain size distribution (e) and distribution of grain boundary misorientations θ (f). For comparison, Fig. 4 (a) shows the EBSD map of standard EUROFER97.

As shown in Fig. 4 (a), standard EUROFER97 steel exhibits a nearly random grain orientation testified by the variety of colors on the map. More precisely, there is a slight [1 1 0] texture of approximately 1.2 times higher than the random state. The microstructure of the steel after the novel treatment has a more refined structure (Fig. 4 b) consisting of fine equiaxed grains with mean size of 600 ± 60 nm and log-normal distribution (Fig. 4 e), which is typical of a recrystallized material. It is noteworthy that the mean grain size is larger (~3 times) than that of coherently diffracting domains determined by XRD. From the literature (e.g. see ref. [40]) it is well-known that crystallite size obtained from XRD analysis is generally smaller than the average grain size obtained with other techniques, especially for metals subjected to high plastic deformation. In this case the difference between the values determined from XRD and EBSD depends on the capability of XRD to distinguish dislocation cells that are misoriented with respect to each other by less

Table 3
Relative intensities of XRD peaks of EUROFER97 steel after the novel treatment and those of Fe with randomly oriented grains (file 6-696 of JCPDS database).

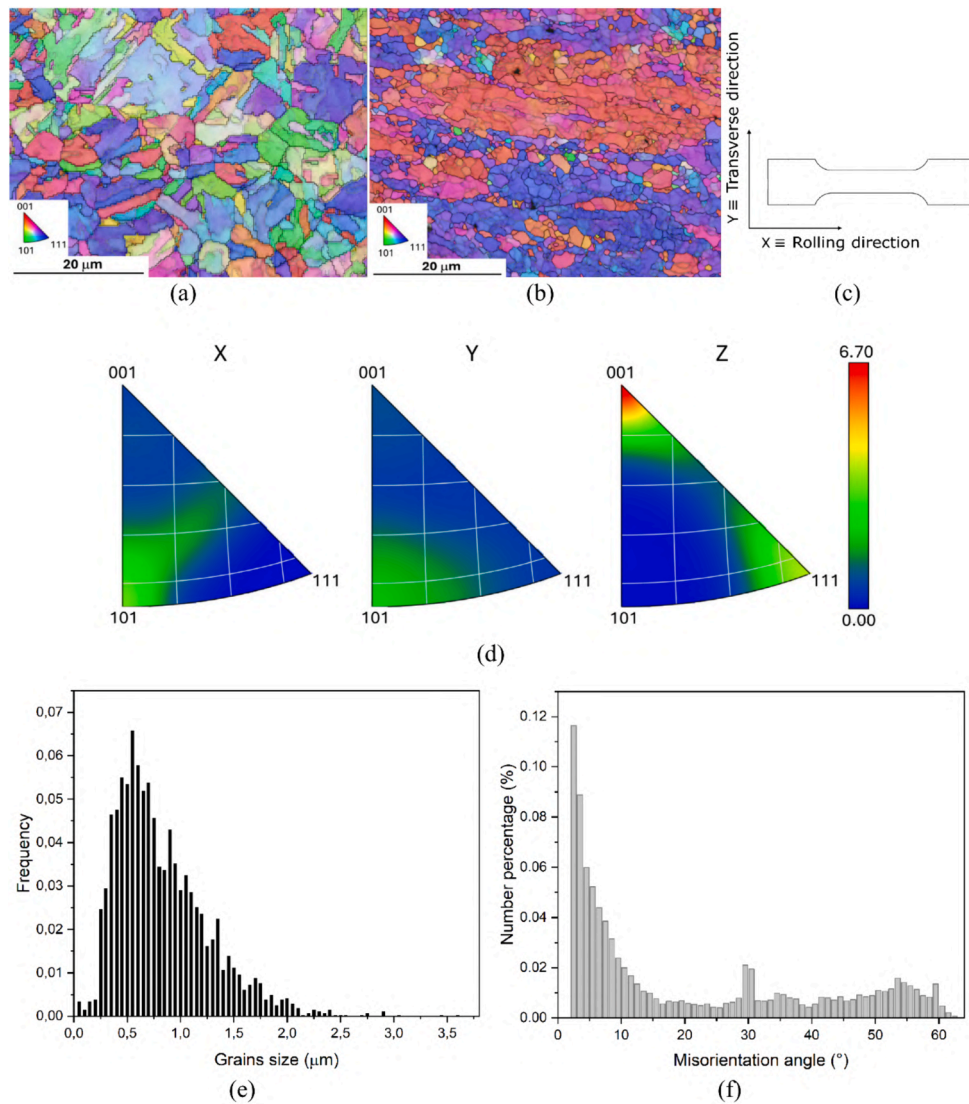| Peaks	110	200	211	220	310	222
JCPDS database- file 6-696	100	20	30	10	12	6
CR:80 % / 650 °C, 1 h	100	66	55	6	9	4

Fig. 4. EBSD map of standard EUROFER97 (a). EUROFER97 after the novel process (CR 80 %/650 °C, 1 h): EBSD map (b) collected on the XY plane of the fatigue sample (c), inverse polar figures (d), grain size distribution (e) and distribution of grain boundary misorientations (f). The Z direction is along the sample thickness.

Table 4
Results of the fatigue tests arranged at increasing σmax.

ID	σmax [MPa]	σmin [MPa]	Δσ [MPa]	Outcome	Observed life
2	366	73	293	10,000,000	Run-out
6	380	76	304	10,000,000	Run-out
5	400	80	320	2,082,200	Failure
12	400	80	320	10,000,000	Run-out
1	422	84	338	472,000	Failure
14	422	84	338	10,000,000	Run-out
4	440	88	352	176,200	Failure
3	449	90	359	224,000	Failure
8	460	92	364	558,500	Failure
11	460	92	368	89,900	Failure
7	480	96	384	70,400	Failure
9	480	96	384	165,300	Failure
10	480	96	384	237,900	Failure
13	500	100	400	48,800	Failure

than 2 degrees.

Inverse polar figures (Fig. 4 d), indicate a [0 0 1] texture in agreement with XRD results displayed in Fig. 3. As evident in Fig. 4 b, the grains with the dominant [0 0 1] orientation (red color) are alternated by bands of grains with the [1 1 1] orientation (blue color). The distribution of grain boundary misorientations (Fig. 4 f) evidences that both high-angle grain boundaries (HAGBs, $\theta > 10°$) and low-angle grain boundaries (LAGBs, $2 < \theta \leq 10°$) are present with a slight prevalence of HAGBs ($\simeq$ 55 %).

3.2. Fatigue tests

The results of the fatigue trials are collected in Table 4.

According to the linear model in the logarithmic scale complying with [31] the S-N curve (for 50 % failure probability) is displayed in Fig. 5.

The General Linear Test confirmed that the linear model is the most suitable for this data distribution. 90 % and 10 % failure probability bounds are also plotted in the same diagram. All the coefficients for the S-N curve and related bounds are reported in Table 5, according to Eq. (8):

$$Log(N) = b_0 + b_1 \bullet Log(S) \pm k \bullet \sigma \qquad (8)$$

Bounds are parallel to the S-N curve and shifted by $k\sigma$, where k is a coefficient reported in [28], which takes into account 90 % confidence and the number of degrees of freedom that is, in turn, related to the
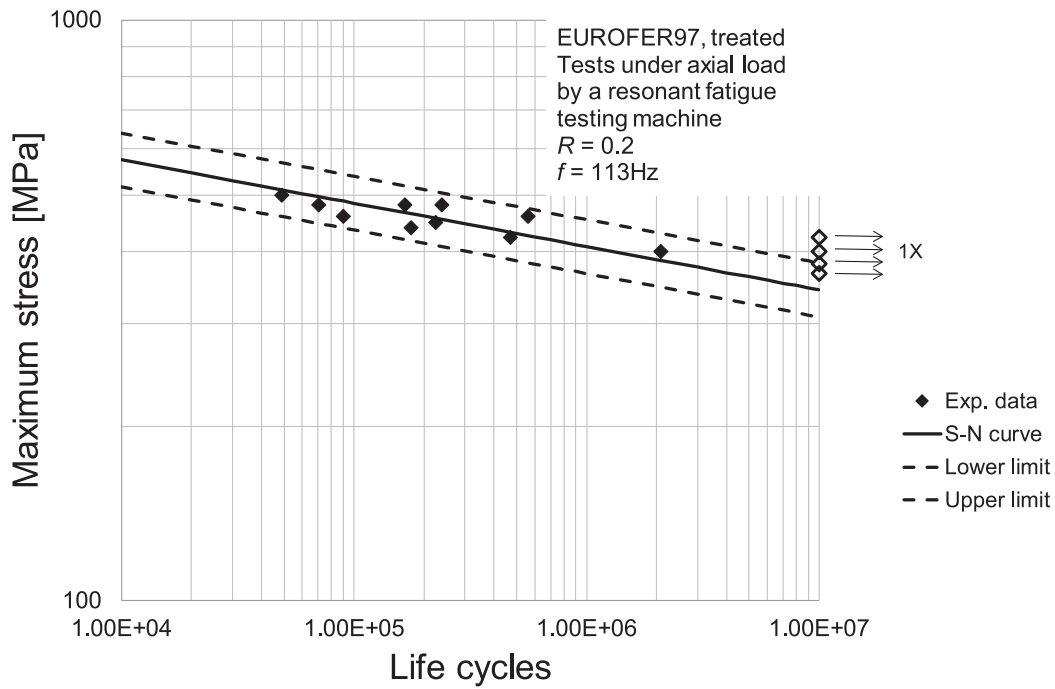
Fig. 5. S-N curve (maximum stress vs. lifespan) according to the linear model.

Table 5
Coefficients of the determined S-N curve and related bounds, according to the linear model in Eq. (8), complying with [31].

b₀	b₁	k·σ
40.982	−13.403	0.621

number of failure data points. σ indicates the standard deviation of the logarithm of fatigue life that depends on the scattering of the observed results and the number of trials.

The S-N curve determined through the MLE approach is shown in Fig. 6.

It is worth mentioning that the sloping part is well consistent with the outcome of the previous interpolation method. As exposed above, a remarkable advantage of this method is related to its ability to estimate the fatigue limit for infinite life, which is around 410 MPa in terms of maximum stress. This outcome can be related and compared to literature values and is of fundamental relevance to evaluate the effect on fatigue behavior of the novel process [19] in comparison to the standard one. Literature data are generally available as fatigue strengths under alternate symmetric load. For instance, a fatigue limit for infinite life may be roughly estimated for many metallic materials as 50 % of *UTS*, e.g. see
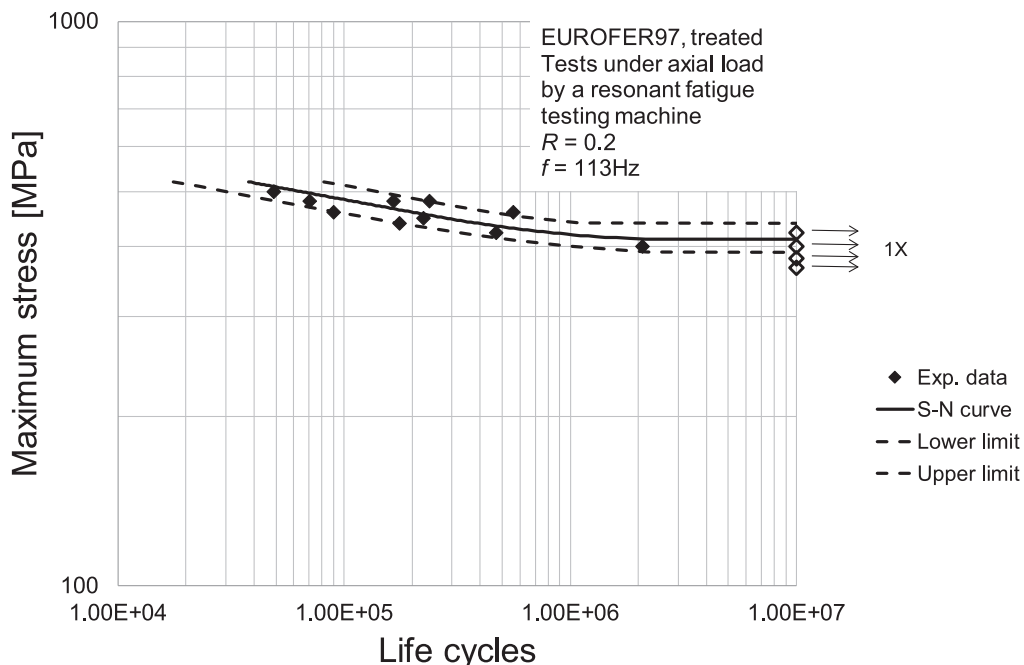

Fig. 6. S-N curve (maximum stress vs. lifespan) according to the MLE approach.

Fig. 7. Wöhler curve: strength for alternate symmetric load plotted vs. lifespan for EUROFER97 following the novel treatment and the conventional one [24].

ref. [41]. In addition, a fatigue strength in the finite life domain for standard EUROFER97 may be worked out from the results in [23,24], which makes it possible to compare the effect of the novel treatment from the point of view of the fatigue response. However, the fatigue strength estimated through the results in [23,24] is again in terms of alternate symmetric load.

Consequently, a conversion is needed through the tool of the Haigh diagram. The fatigue strength in terms of maximum stress is given by the Goodman relation in Eq. (9):

$$S = S_{max} = (1 + R^*) \cdot \frac{S_n}{R^* + \frac{S_n}{UTS}} \tag{9}$$

where S_n is the fatigue strength for alternate symmetric load and R^* is the ratio between the stress amplitude and the mean stress (for load ratio $R = 0.2$, $R^* = 0.67$). In order to enable comparisons, the formula in Eq. (9) must be rearranged as in Eq. (10), to determine S_n as a function of S_{max}.
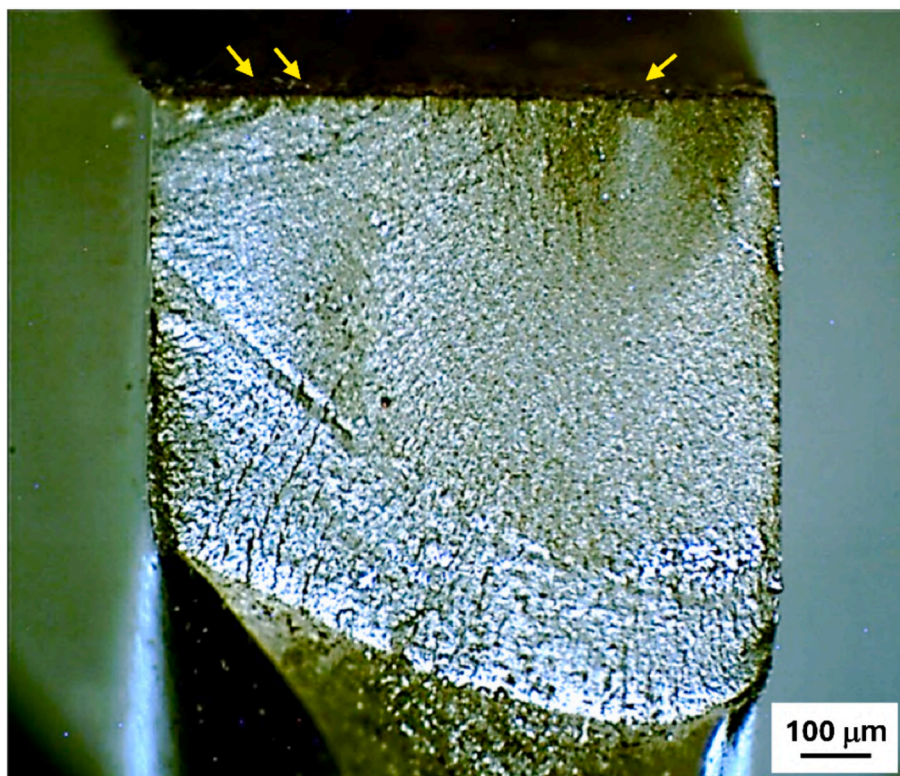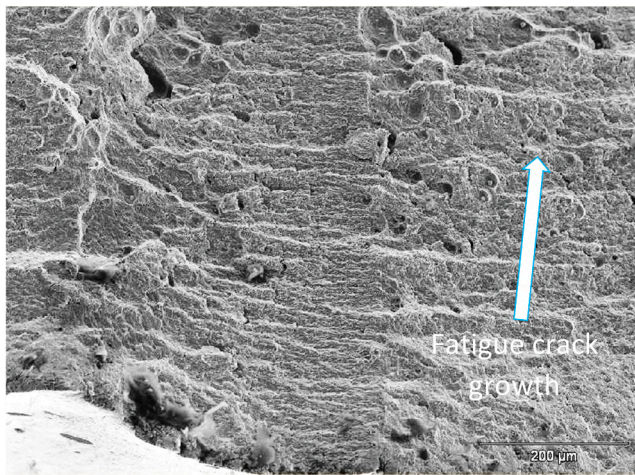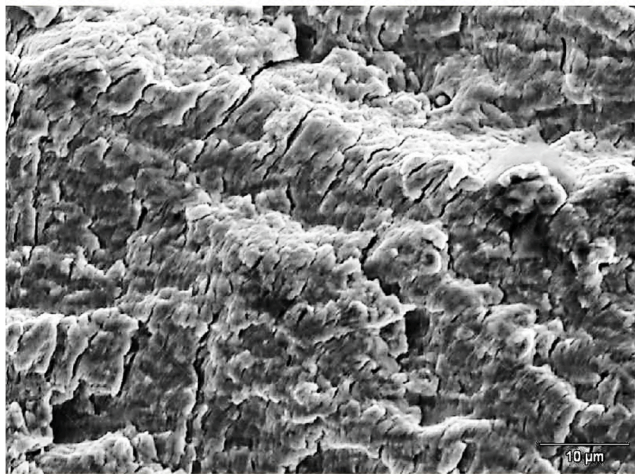

Fig. 8. SM image of the fracture surface of sample #5 (see Table 4). Crack nucleation sites are indicated by yellow arrows. (For interpretation of the references to color in this figure legend, the reader is referred to the web version of this article.)

(a)

(b)

Fig. 9. SEM micrographs of the fracture surface of sample #5.

$$S_n = \frac{R^* \bullet UTS \bullet S_{max}}{(1 + R^*) \bullet UTS - S_{max}} \qquad (10)$$

By introducing $S_{max} = 410 MPa$ in Eq. (10), $S_n = 255 MPa$ is obtained. This value indicates the estimated fatigue limit (for infinite life) for EUROFER97 treated by the novel treatment under alternate symmetric load. S_n is indeed lower than half of the material UTS, and around $0.37 \cdot$UTS. However, this value appears to be well aligned with that of many highly alloyed heat-treated steels [41].

As highlighted in the Introduction Section, the LCF characterization made in [23] and [24] led to an estimated life of 30,000–100,000 cycles (i.e., at the boundaries of the commonly accepted lifespan for LCF) for an elastic strain amplitude a bit lower than 0.2 % under alternate symmetric load. In addition, applying the Hooke's law for the uniaxial stress state, this strain amplitude can be converted into a strength for alternate load, namely S_n. Thus, as highlighted above, the availability of this curve makes it possible to compare the performance of EUROFER97 with the novel treatment to that of the same material after the standard treatment. For this purpose, the curve in Fig. 6 has been rearranged: for the number of cycles in the observed lifespan, corresponding values of strength in terms of the maximum stress S_{max} have been introduced in Eq. (10), thus determining the estimated strengths for alternate load S_n. These values have then been used to determine a new Wöhler curve, where the estimated strength for alternate symmetric load is plotted versus life cycles. For comparison purposes, the curve in [24] (for the available lifespan) and the just mentioned Wöhler curve are plotted
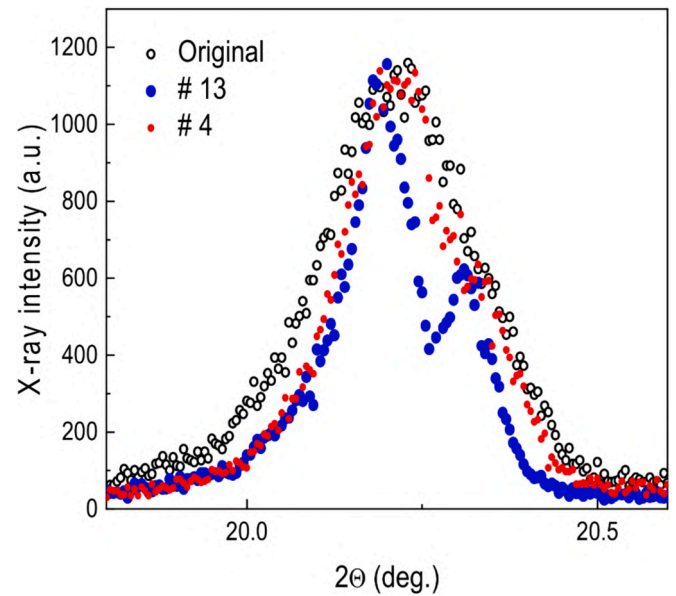

Fig. 10. {1 1 0} XRD peak profiles of the original material (before fatigue tests) and of samples #4 and #13.

together in the same diagram in Fig. 7. It is worth mentioning the curve taken from [24] is within the boundaries of the here determined curve and that the fatigue strengths are very close, with a maximum difference in the order of 5 % (350 MPa at 10^5 cycles for the conventionally heat treated EUROFER97 and 335 MPa at the same life extent following the novel treatment). Therefore, it can be concluded the novel process described in [19] leads to significant enhancements from the point of view of the static mechanical behavior of EUROFER97, in particular high ductility and yield point, and does not worsen the fatigue response.

3.3. Microstructural examination of the material after fatigue tests

The fracture surfaces were at first examined by means of SM observations. The SM images, like that displayed in Fig. 8, reveal that preferred crack nucleation sites, indicated by yellow arrows, are generally surface imperfections due to the fabrication process of probes. Since the presence of inclusions in EUROFER97 steel is negligible, subsurface crack nucleation were not observed.

The fracture surfaces were investigated by SEM observations. As well known, fatigue consists of three different stages [42]: (stage I), initiation of the crack; (stage II), propagation of the crack due to the cyclic load; and (stage III), the very fast growth of the fracture up to final failure, when the cross section can no longer withstand the load. The microstructural features observed in fatigued samples under different stresses do not exhibit relevant differences and an example is shown in Fig. 9.

In all the analyzed surfaces, the stage I zone was insufficiently defined to perform a deep characterization. On the contrary, stage II is very well defined and fracture surfaces exhibit the typical striation marks produced in a ductile material with regular size and spacing of about 10 µm (Fig. 9 a). As displayed in Fig. 9 (b) at higher magnification, cracks are perpendicular to the striation marks, while no crack nucleation at carbide interfaces or even cleavage in secondary phases were observed.

XRD measurements carried out on the samples after fatigue tests show that peak profiles become significantly narrower with respect those of original material. This is clearly displayed by the example in Fig. 10, where the {1 1 0} XRD peak profile of the original material is compared with those of samples #4 and #13 (Table 4). The peak intensities have been normalized to favor the comparison. Since no monochromator has been used in present XRD experiments each peak is

Table 6

Samples broken in fatigue tests: β_T (2θ) of {110} peak after experimental broadening subtraction. The σmax values of the samples are reported too.

ID	# 5	# 1	# 4	# 3	# 8	# 11	# 7	# 9	# 10	# 13
β_T [2θ degrees]	0.050	0.055	0.095	0.105	0.100	0.085	0.100	0.053	0.065	0.050
σmax [MPa]	400	422	440	449	460	460	474	480	480	500

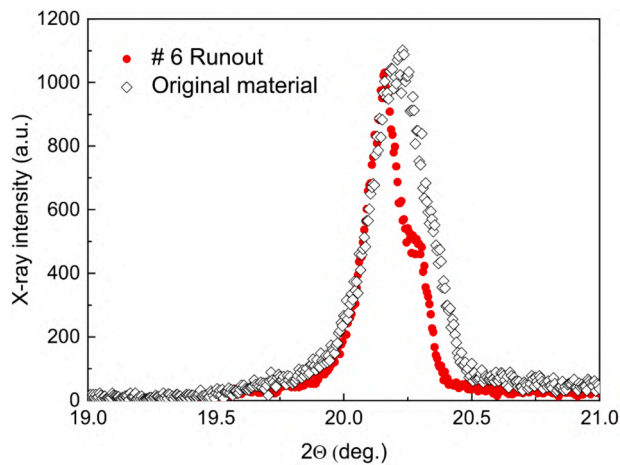**Fig. 11.** {110} XRD peak profiles of the original material and sample # 6 (run-out).

the overlapping of the Kα1 and Kα2 contributions. In the case of sample #13 narrowing is so pronounced that the two contributions, Kα1 and Kα2, can be clearly distinguished.

The β_T values reported in Table 6 have been determined by separating the two contributions and subtracting the instrumental broadening from FWHM of the Kα1 one. β_T, expressed in 2θ degrees, of all the fatigued samples are always remarkably lower than that of the original material (0.125°). Even if there is some scattering of data, peak narrowing tends to be more pronounced for increasing maximum stress upon cycling.

It is noteworthy that the not broken samples (run-out) also exhibit a significant peak narrowing. An example is shown in Fig. 11: the {110} peak profile of the original material is quite broader than that of sample # 6.

XRD results indicate that stress in fatigue tests induces instability of dislocation structures forming the grain boundaries. Such instability leads to the collapse of some grain boundaries with consequent partial annihilation and re-arrangement of dislocations, and grain coalescence. The effect seems to depend on the applied stress because β_T values exhibit a tendency to decrease as σmax increases. The problem of the instability in dislocation structures has not been completely understood yet and different theoretical approaches have been proposed (e.g., see refs. [43–45]). Anyway, the processes of partial annihilation and re-arrangement of dislocations tend to minimize the internal energy of the solid under dynamic conditions; thus, the synergy of dislocations and the applied stress plays a decisive role. Since the investigated material is fully recrystallized, it is supposed that instability could be triggered by grain boundary migration, namely the collective motion of dislocations forming the boundary, induced by the applied stress. When two boundaries encounter the excess of dislocations, it makes the new boundary unstable and leads to its collapse. This tentative explanation must be verified in the future through systematic transmission electron microscopy (TEM) observations. Anyway, a similar phenomenon has been already observed by one of present investigators in Al alloys [46] and superalloys [47] during heat treatments.

To get more information about grain evolution, EBSD data have been collected on the fatigued samples by examining the zones near the fracture. For example, Fig. 12 displays the EBSD map (a), the analysis of grain boundary type (b), the inverse polar figures (c), the distributions of grain size (d) and grain boundary misorientations (e) of sample #13.

By comparing the data in Fig. 4 (original material) and Fig. 12 (sample #13), the differences are evident. In particular, after fatigue testing, the mean grain size is larger (873 ± 53 nm) than the original one (600 ± 60 nm) and some texture change occurs.

Moreover, from the analyses of EBSD maps the relative fraction of LAGBs decreases from 0.45 ± 0.01 (original material) to 0.36 ± 0.05 (sample #13). It is observed that LAGBs are dominant in the areas where grains exhibit the larger size (Fig. 12 b). In the original material there is a large amount of LAGBs (Fig. 4 e), and EBSD shows that mainly these boundaries become unstable under stress in fatigue tests.

KAM were also collected to reveal local dislocation structures, however slight differences were observed in fatigued samples compared to the original material. For example, Fig. 13 shows the KAM maps to the 3rd neighbor with 5° threshold angle of the original material (a) and fatigued sample #13 (c); the corresponding distributions of misorientation angles are displayed in (b) and (d), respectively. The average KAM angle rises from 0.32° to 0.37° after fatigue testing.

XRD patterns collected on samples broken in fatigue tests by focusing the X-ray beam near the crack (~1 mm) are displayed in Fig. 14 while Table 7 reports the relative intensities of the most intense peaks.

The ratios between the intensities of the strongest XRD reflections, I_{200}/I_{110} and I_{211}/I_{110}, evidence that grain growth induces texture variations: the [100] cubic texture of the original material is still retained, however its intensity changes. In large part of the samples, it results to be stronger, in some samples (#8, #10, #11) it weakens without a specific relation between texture variations and maximum applied stress σmax.

The microstructure evolution also corresponds to a change in hardness. In Fig. 15 hardness values measured in samples after fatigue tests are plotted vs. Δσ: even if a certain scattering of data is observed, hardness tends to decrease as Δσ increases. Anyway, all data are lower than that of the original material with variations up to 8 %. The continuous red line is the average value from measures in different sheet positions, while the dashed lines represent the maximum data scattering.

The hardness values reported in Fig. 15 were taken near the crack. In order to assess whether the observed effects are not local artifacts, measurements were carried out along the axis of the samples. The results showed that, as the distance from the crack increases, hardness tends to decrease. Generally, such decrease is small, in the order of 1–2 % at a distance of 3.5 mm, and can be explained as a deformation of the metal along the crack path. Therefore, softening is not an artifact but an effect of fatigue.

Grain growth driven by stress below the homologous temperature has already been observed in nanocrystalline materials under various loading conditions such as tensile [48,49], compression [50], indentation [51,52], and fatigue tests [53–55]. The homologous temperature of EUROFER97, defined as $T/T_M = 0.5$ (solidus temperature $T_M = 1447$ °C [56]) is 587 °C. Grain boundaries, especially LAGBs, can migrate owing to the collective motion of dislocations induced by the applied stress. To the best of our knowledge, only one case of fatigue-assisted grain growth at room temperature in 7075 Al alloy has been reported in the literature for metal alloys with an average grain size in the order of hundreds of nanometers or micrometers [57]. Therefore, the phenomenon observed in the present work represents a novelty of great interest because investigating and quantitatively assessing the microstructural stability of this steel is of the utmost relevance for nuclear applications.
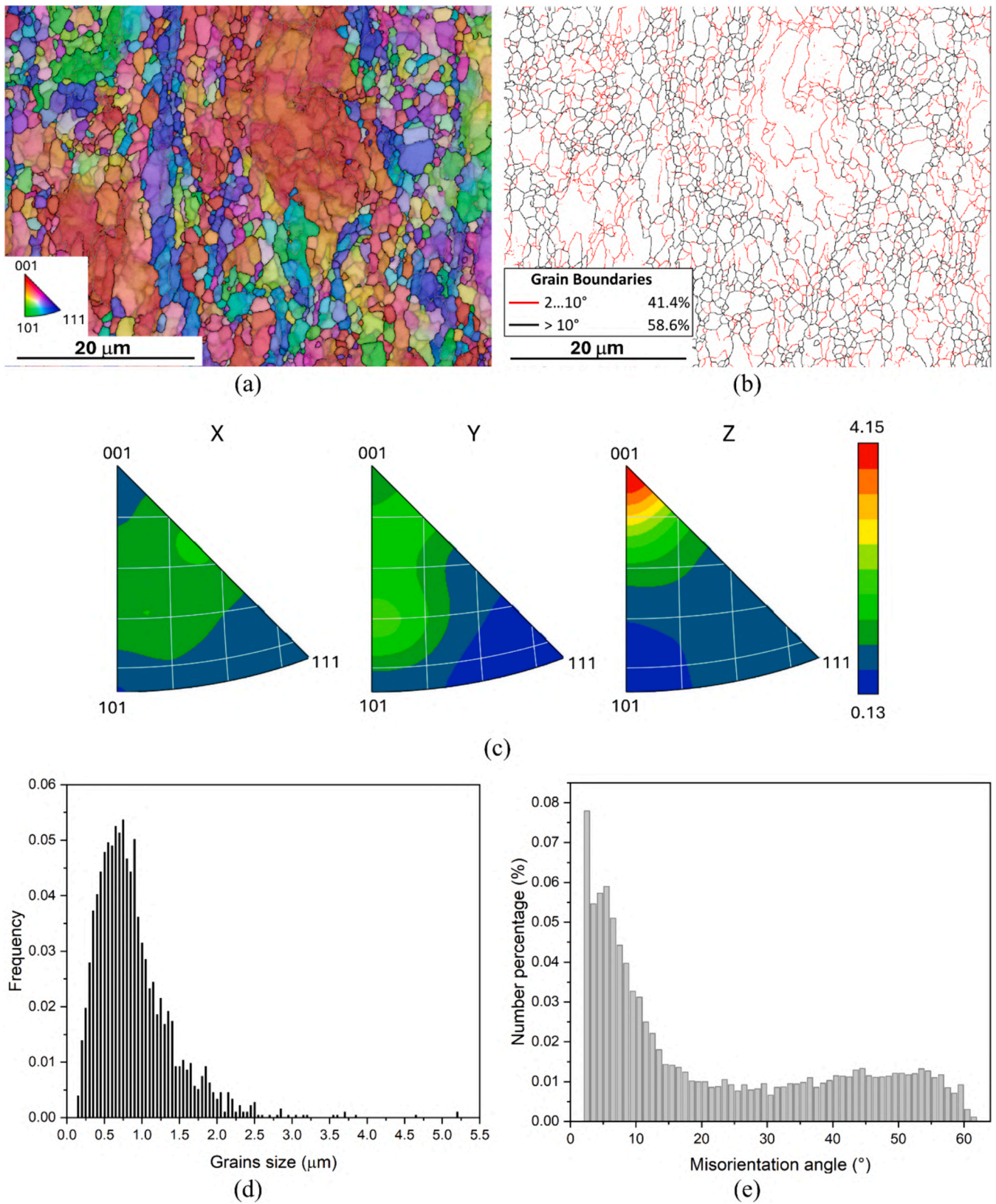
Fig. 12. Sample #13: EBSD map collected on the plane XY (a), analysis of grain boundary type (LAGBs 2-10°; HAGBs > 10°) (b), inverse polar figures (c), grain size distribution (d) and distribution of grain boundary misorientations (e).
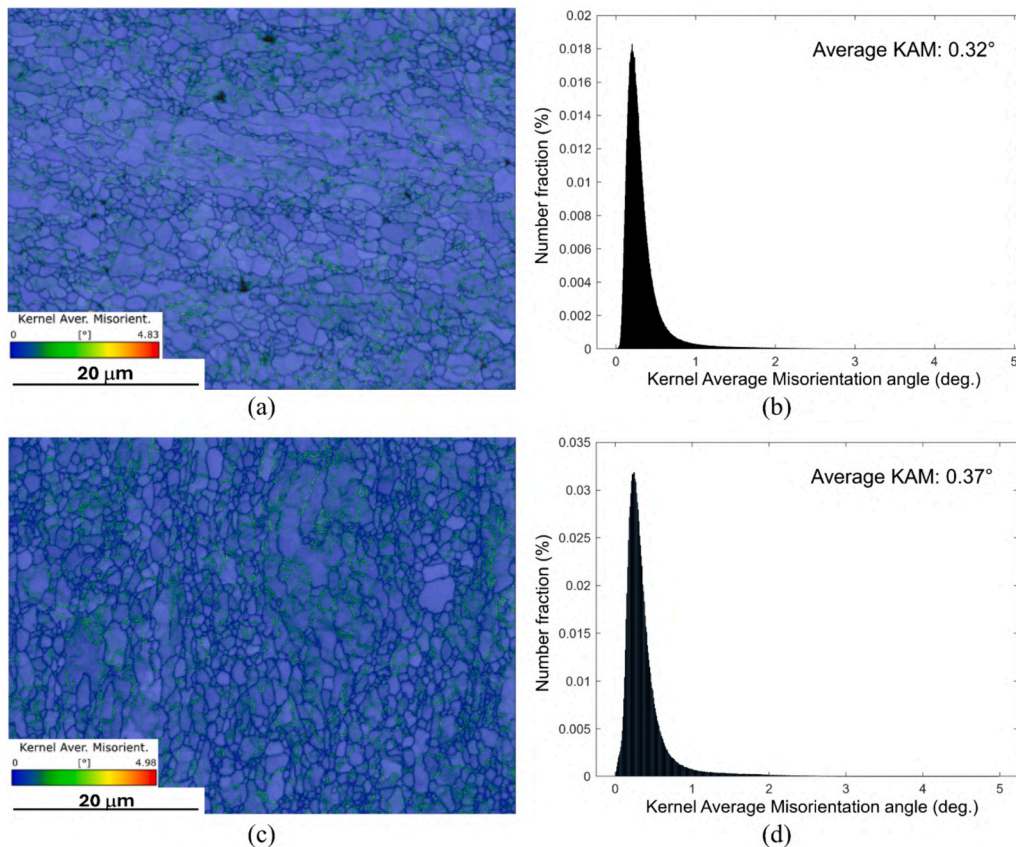
Fig. 13. KAM maps of original material (a) and fatigued sample #13 (c). The corresponding distributions of misorientation angles are displayed in (b) and (d), respectively.
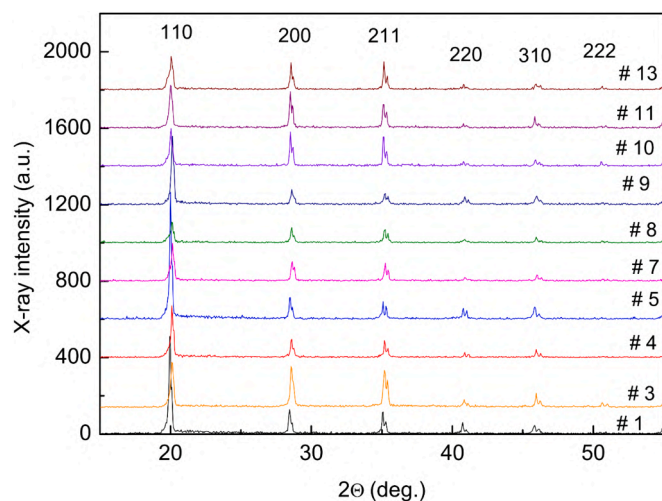

Fig. 14. XRD patterns of EUROFER97 samples broken in fatigue tests.

Moreover, present results suggest having a close check on standard EUROFER97 steel. Indeed, it also exhibits a large number of LAGBs: based on our measurements, the relative amount of LAGBs is ~38 %, whereas Barcelo et al. [58] found a little smaller value (32 %). Although the microstructure of standard EUROFER97 (laths of tempered martensite inside prior austenite grains, PAGs) is different from that originated by the novel process developed by us, its fraction of LAGBs is significant. It is noteworthy that, in LCF testing, Giordana et al. [59] and Kuběna et al. [60] observed a pronounced softening of EUROFER97 steel that is also accompanied by microstructural changes, such as the

decrease of free dislocations inside the sub-grains. Moreover, after LCF experiments carried out from room temperature up to 300 °C, Marmy et al. [23] observed that large grains were fractioned into fatigue cells and dislocation density decreases. Dislocations are swept out to the grain/subgrain boundaries by the cyclic plastic deformation and may be observed mainly in small grains or inside some grains attached and pinned by precipitates. On these grounds, previous results of fatigue tests carried out on standard EUROFER97 should be reconsidered to assess the possible occurrence of grain growth driven by stress in fatigue conditions.

4. Conclusions

The present paper has investigated the high cycle fatigue behavior of EUROFER97 steel submitted to a novel process consisting of cold rolling with reduction ratio of 80 % followed by heat treatment at 650 °C for 1 h. The main results can be resumed as follows.

1. The fatigue strength of the steel submitted to the novel process is comparable, within experimental errors, to that of the standard EUROFER97.
2. Fracture surfaces exhibit the typical striation marks produced in a ductile material with regular size and spacing of about 10 μm. Cracks are perpendicular to the striation marks, while no crack nucleation at carbide interfaces or even cleavage in secondary phases were observed.
3. The fatigued samples underwent a microstructural evolution consisting of grain size increase and texture change.
4. The microstructural transformation is attributed to the stress-driven instability of grain boundaries, especially LAGBs, leading to the

Table 7

Relative intensities of XRD peaks of EUROFER97 samples broken in fatigue tests arranged with increasing σmax. The values of the original material (O.M.) are reported for comparison.

| ID	σmax [MPa]	Peaks						Intensity ratio	
		110	200	211	220	310	222	I_{200}/I_{110}	I_{211}/I_{110}
O.M.	–	100	66	55	6	9	4	0.66	0.55
5	400	100	17	14	9	4	2	0.17	0.14
1	422	100	23	22	8	10	6	0.23	0.22
4	440	100	35	33	7	10	13	0.35	0.33
3	449	100	61	54	17	15	6	0.61	0.54
8	460	100	74	64	17	28	20	0.74	0.64
11	460	100	85	53	10	24	4	0.85	0.53
7	474	100	55	53	10	16	10	0.55	0.53
9	480	100	27	24	14	13	4	0.27	0.24
10	480	100	93	71	11	15	8	0.93	0.71
13	500	100	52	38	10	12	4	0.52	0.38
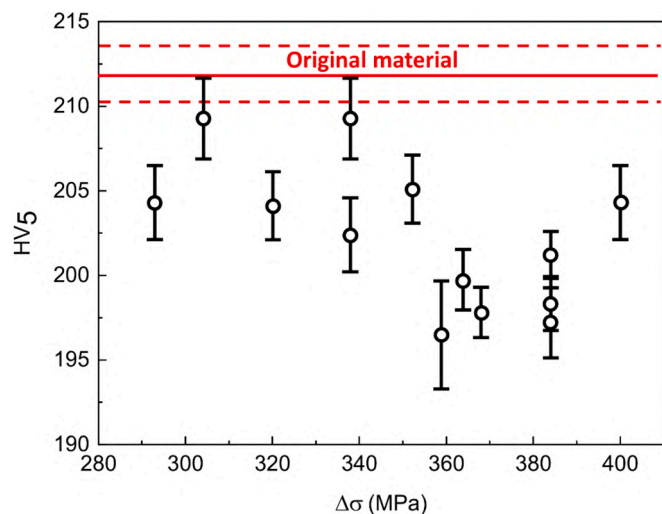
Fig. 15. Hardness of samples submitted to fatigue tests vs. Δσ. The continuous red line is the average value from measures in different sheet positions while the dashed lines represent the maximum data scattering. (For interpretation of the references to color in this figure legend, the reader is referred to the web version of this article.)

collapse of some boundaries with consequent partial annihilation and re-arrangement of dislocations, and grain coalescence.

5. Softening occurs in fatigued samples with variations up to 8 %; hardness generally tends to decrease as Δσ increases.

CRediT authorship contribution statement

Dario Croccolo: Writing – review & editing, Methodology, Investigation, Formal analysis, Data curation. **Andrea Di Schino:** Writing – review & editing, Resources, Investigation, Formal analysis, Data curation. **Roberto Montanari:** Writing – review & editing, Writing – original draft, Supervision, Formal analysis, Data curation, Conceptualization. **Giorgio Olmi:** Writing – review & editing, Writing – original draft, Supervision, Methodology, Investigation, Formal analysis, Data curation. **Giulia Stornelli:** Writing – review & editing, Resources, Project administration, Investigation, Formal analysis, Data curation, Conceptualization. **Claudio Testani:** Writing – review & editing, Resources, Investigation, Formal analysis, Data curation. **Alessandra Varone:** Writing – review & editing, Project administration, Investigation, Formal analysis, Data curation, Conceptualization.

Declaration of competing interest

The authors declare that they have no known competing financial interests or personal relationships that could have appeared to influence the work reported in this paper.

Data availability

The data that has been used is confidential.

References

[1] Tavassoli AAF, Alamo A, Bedel L, Forest L, Gentzbittel JM, Rensman JW, et al. Materials design data for reduced activation martensitic steel type EUROFER. J Nucl Mater 2004;329–333(257–262). https://doi.org/10.1016/j.jnucmat.2004.04.020.

[2] Hoffmann J, Rieth M, Commin L, Fernández P, Roldán M. Improvement of reduced activation 9%Cr steels by ausforming. Nucl Mater Energy 2016;6:12–7. https://doi.org/10.1016/j.nme.2015.12.001.

[3] Stornelli G, Rallini M, Testani C, Montanari R, Di Schino A. Effects of thermo-mechanical treatments on EUROFER97 steel for applications in nuclear fusion reactors. La Metallurgia Italiana 2020;112:34–44.

[4] Chen X, Bhattacharya A, Sokolov MA, Clowers LN, Yamamoto Y, Graening T, et al. Mechanical properties and microstructure characterization of Eurofer97 steel variants in EUROfusion program. Fusion Eng Des 2019;146:2227–32. https://doi.org/10.1016/j.fusengdes.2019.03.158.

[5] Gaganidze E, Gillemot F, Szenthe I, Gorley M, Rieth M, Diegele E. Development of EUROFER97 database and material property handbook. Fusion Eng Des 2018;135:9–14. https://doi.org/10.1016/j.fusengdes.2018.06.027.

[6] Montanari R, Filacchioni G, Iacovone B, Plini P, Riccardi B. High temperature indentation tests on fusion reactor candidate materials. J Nucl Mater 2007;367–370:648–52. https://doi.org/10.1016/j.jnucmat.2007.03.099.

[7] Stornelli G, Montanari R, Testani C, Pilloni L, Napoli G, Di Pietro O, et al. Microstructure refinement Effect on EUROFER 97 steel for nuclear fusion application. Mater Sci Forum 2021;1016:1392–7. https://doi.org/10.4028/www.scientific.net/MSF.1016.1392.

[8] Montanari R, Filacchioni G, Riccardi B, Tata ME, Costanza G. Characterization of EUROFER 97 TIG-welded joints by FIMEC indentation tests. J Nucl Mater 2004;1529:329–33. https://doi.org/10.1016/j.jnucmat.2004.04.173.

[9] Lindau R, Möslang A, Rieth M, Klimiankou M, Materna-Morris E, Alamo A, et al. Present development status of EUROFER and ODS-EUROFER for application in blanket concepts. Fusion Eng Des 2005;8:75–9. https://doi.org/10.1016/j.fusengdes.2005.06.186.

[10] Coppola R, Klimenkov M. Dose dependence of micro-voids distributions in low-temperature neutron irradiated Eurofer97 steel. Metals 2019;9:552. https://doi.org/10.3390/met9050552.

[11] Roldán M, Fernández P, Rams J, Jiménez-Rey D, Ortiz CJ, Vila R. Effect of helium implantation on mechanical properties of EUROFER97 evaluated by nanoindentation. J Nucl Mater 2014;448:301–9. https://doi.org/10.1016/j.jnucmat.2014.02.020.

[12] Roldán M, Fernández P, Rams J, Jiménez-Rey D, Materna-Morris E, Klimenkov M. Comparative study of helium effects on EU-ODS-EUROFER and EUROFER97 by nanoindentation and TEM. J Nucl Mater 2015;460:226–34. https://doi.org/10.1016/j.jnucmat.2015.02.025.

[13] Fu J, Brouwer J, Hendrikx R, Richardson I, Hermans M. Microstructure characterisation and mechanical properties of ODS-Eurofer steel subject to

designed heat treatments. Mater Sci Eng A 2020;770:138568. https://doi.org/10.1016/j.msea.2019.138568.

[14] De Sanctis M, Fava A, Lovicu G, Montanari R, Richetta M, Testani C, et al. Mechanical characterization of a nano-ODS steel prepared by low-energy mechanical alloying. Metals 2017;7:283. https://doi.org/10.3390/met7080283.

[15] Zinkle SJ, Möslang A. Evaluation of irradiation facility options for fusion materials research and development. Fusion Eng Des 2013;88:472–82. https://doi.org/10.1016/j.fusengdes.2013.02.081.

[16] Beyerlein IJ, Caro A, Demkowicz MJ, Mara NA, Misra A, Uberuaga BP. Radiation damage tolerant nanomaterials. Mater Today 2013;16:443–9. https://doi.org/10.1016/j.mattod.2013.10.019.

[17] Song M, Wu YD, Chen D, Wang XM, Sun C, Yu KY, et al. Response of equal channel angular extrusion processed ultrafine-grained T91 steel subjected to high temperature heavy ion irradiation. Acta Mater 2014;74:285–95. https://doi.org/10.1016/j.actamat.2014.04.034.

[18] Stornelli G, Di Schino A, Montanari R, Testani C, Varone A. Assessment of Mechanical Properties and Microstructure of EUROFER97 Steel after Thermo-Mechanical Treatments. Mater Sci Forum 2023;1105:47–52. https://doi.org/10.4028/p-t3IMA9.

[19] Stornelli G, Di Schino A, Mancini S, Montanari R, Testani C, Varone A. Grain refinement and improved mechanical properties of EUROFER97 by thermo-mechanical treatments. Appl Sci 2021;11:10598. https://doi.org/10.3390/app112210598.

[20] Schuring EW, Hofmans HE. Metallographic characterization of EUROFER97 plate and bar materials. Report ECN Library; 2000.

[21] Qiu GX, Zhan DP, Cao L, Jiang ZH. Review on development of reduced activated ferritic/martensitic steel for fusion reactor. J Iron Steel Res Int 2022;29:1343–56. https://doi.org/10.1007/s42243-022-00796-2.

[22] Lindau R, Möslang A, Rieth M, Klimiankou M, Materna-Morris E, Alamo A, et al. Present development status of EUROFER and ODS-EUROFER for application in blanket concepts. Fusion Eng Des 2005;75–79:989–96. https://doi.org/10.1016/j.fusengdes.2005.06.186.

[23] Marmy P, Kruml T. Low cycle fatigue of Eurofer 97. J Nucl Mater 2008;377(1):52–8. https://doi.org/10.1016/j.jnucmat.2008.02.054.

[24] Roldán M, Leon-Gutierrez E, Fernández P, Gómez-Herrero A. Deformation behaviour and microstructural evolution of EUROFER97-2 under low cycle fatigue conditions. Mater Charact 2019;158:109943. https://doi.org/10.1016/j.matchar.2019.109943.

[25] Walter M, Aktaa J, Lerch M. Failure behaviour of EUROFER 97 in the low-cycle fatigue region under multi-step loading. Int J Fatigue 2008;30:568–73. https://doi.org/10.1016/j.ijfatigue.2007.03.001.

[26] Weick M, Aktaa J. Multiaxial fatigue behavior of EUROFER 97. J Nucl Mater 2007;367–370:633–6. https://doi.org/10.1016/j.jnucmat.2007.03.101.

[27] Petersen C, Povstyanko A, Prokhorov V, Fedoseev A, Makarov O, Walter M. Tensile and low cycle fatigue properties of different ferritic/martensitic steels after the fast reactor irradiation 'ARBOR 1'. J Nucl Mater 2009;386–388:299–302. https://doi.org/10.1016/j.jnucmat.2008.12.112.

[28] Luzginova NV, Rensman J, Pierick P, Hegeman JBJ. Low cycle fatigue of irradiated and unirradiated Eurofer97 steel at 300 °C. J Nucl Mater 2011;409:153–5. https://doi.org/10.1016/j.jnucmat.2010.09.017.

[29] Rieth M, Schirra M, Falkenstein A, Graf P, Heger S, Kempe H, Lindau R, Zimmermann H. EUROFER 97 Tensile, Charpy, Creep and Structural Tests; Report FZKA6911, Eurofusion Programme; Forschungzentrum Karlsruhe g.m.b.h.: Karlsruhe, Germany; 2003.

[30] International Organization for Standardization ISO 1143:2010. Standard - Metallic materials - Rotating bar bending testing. Geneva, Switzerland: International Organization for Standardization (ISO); 2010.

[31] International Organization for Standardization ISO 12107:2012. Metallic Materials - Fatigue Testing - Statistical Planning and Analysis of Data. Geneva, Switzerland: International Organization for Standardization (ISO); 2012.

[32] Croccolo D, Bogojevic N, De Agostinis M, Fini S, Olmi G, Robusto F, et al. Fatigue response of additively manufactured as-built 15–5 PH stainless steel and effects of machining and thermal and surface treatments. Fatigue Fract Eng Mater Struct 2023;46(2):433–51. https://doi.org/10.1111/ffe.13875.

[33] Pascual FG, Meeker WQ. Estimating fatigue curves with the random fatigue-limit model. Technometrics 1999;41:277–89. https://doi.org/10.2307/1271342.

[34] Pollak RD, Palazotto AN. A comparison of maximum likelihood models for fatigue strength characterization in materials exhibiting a fatigue limit. Probabilistic Eng Mech 2009;24:236–41. https://doi.org/10.1016/j.probengmech.2008.06.006.

[35] Strzelecki P, Tomaszewski T, Sempruch J. A method for determining a complete S-N curve using maximum likelihood. In: Proceedings of the 22nd International Conference Engineering Mechanics. 2016, Svratka, Czech Republic, 9-12 May 2016.

[36] Loren S, Lundstrom M. Modelling curved S-N curves. Fatigue Fract Eng Mater Struct 2005;28:437–43. https://doi.org/10.1111/j.1460-2695.2005.00876.x.

[37] Croccolo D, Ciric-Kostic S, De Agostinis M, Fini S, Olmi G, Bogojevic N, et al. Effect of the position in the build chamber on the fatigue strength of additively manufactured maraging steel MS1. Machines 2023;11:196. https://doi.org/10.3390/machines11020196.

[38] Williamson GK, Smallman III RE. Dislocation densities in some annealed and cold-worked metals from measurements on the X-ray Debye-Scherrer spectrum. Philos Mag 1956;1:34–46. https://doi.org/10.1080/14786435608238074.

[39] JCPDS. International Centre for Diffraction Data; JCPDS: Newtown Square, PA, USA; 1907.

[40] Ungár T, Tichy G, Gubicza J, Hellmig RJ. Correlation between subgrains and coherently scattering domains. Powder Diff 2005;20:366–75. https://doi.org/10.1154/1.2135313.

[41] Niemann G, Winter H, Hohn BR. Maschinenelemente. Berlin, Germany: Springer Verlag; 2005.

[42] ASM, Fractography. 6. Print Ed. ASM Handbook. Materials Park, Ohio: ASM International. vol. 517; 2009.

[43] Yan Y, Kondo T, Shimada T, Sumigawa T, Kitamura T. Criterion of mechanical instabilities for dislocation structures. Mater Sci Eng A 2012;534:681–7. https://doi.org/10.1016/j.msea.2011.12.027.

[44] Wu R, Tuzes D, Isp'anovity PD, Groma I, Zaiser M. Instability of dislocation fluxes in a single slip: Deterministic and stochastic models of dislocation patterning. Phys Rev B 2017. https://doi.org/10.1103/PhysRevB.98.054110.

[45] Deka N, Alleman C, Douglas L, Medlin DL, Sills RB. Energy and stochasticity: the yin and yang of dislocation patterning. Mater Res Lett 2023;11(4):289–95. https://doi.org/10.1080/21663831.2022.2149283.

[46] Gondi P, Montanari R, Veniali F. Relaxation and X-ray diffraction line broadening phenomena during grain growth of metals. J de Phys 1987;C8–12:429. https://doi.org/10.1051/jphyscol:1987865.

[47] Deodati P, Montanari R, Tassa O, Ucciardello N. Single crystal PWA 1483 superalloy: dislocation rearrangement and damping phenomen. Mater Sci Eng A 2009;521–522:102–5. https://doi.org/10.1016/j.msea.2008.09.107.

[48] Brandstetter S, Zhang K, Escuadro A, Weertman J, Swygenhoven HV. Compression of bulk nanocrystalline nickel and copper. Scr Mater 2008;58:61–5.

[49] Fan GJ, Fu LF, Choo H, Liaw PK, Browning ND. Uniaxial tensile plastic deformation and grain growth of bulk nanocrystalline alloys. Acta Mater 2006;54:4781–92. https://doi.org/10.1016/j.actamat.2006.06.016.

[50] Pan D, Kuwano S, Fujita T, Chen MW. Ultra-large room-temperature compressive plasticity of a nanocrystalline metal. Nano Lett 2007;7:2108–11. https://doi.org/10.1021/nl071093m.

[51] Jin M, Minor AM, Stach EA, Morris Jr JW. Direct observation of deformation-induced grain growth during the nanoindentation of ultrafine-grained Al at room temperature. Acta Mater 2004;52:5381–5. https://doi.org/10.1016/j.actamat.2004.07.044.

[52] Zhang K, Weertman JR, Eastman JA. Rapid stress-driven grain coarsening in nanocrystalline Cu at ambient and cryogenic temperatures. Appl Phys Lett 2005;87:061921. https://doi.org/10.1063/1.2008377.

[53] Hanlon T, Tabachnikova ED, Suresh S. Fatigue behavior of Nano crystalline metals and alloys. Int J Fatigue 2005;27:1147–58. https://doi.org/10.1016/j.ijfatigue.2005.06.035.

[54] Gianola DS, Eberl C, Cheng XM, Hemker KJ. Stress-driven surface topography evolution in nanocrystalline Al thin films. Adv Mater 2008;20:303–8. https://doi.org/10.1002/adma.200701607.

[55] Meirom RA, Alsem DH, Romasco AL, Clark T, Polcawich RG, Pulskamp JS, et al. Fatigue-induced grain coarsening in nanocrystalline platinum films. Acta Mater 2011;59:1141–9. https://doi.org/10.1016/j.actamat.2010.10.047.

[56] Oliveira VB, Zilnyk KD, Sandim HRZ. Thermodynamic simulation of reduced activation ferritic–martensitic Eurofer-97 steel. J Phase Equilib Diffus 2017;38:208–16. https://doi.org/10.1007/s11669-017-0530-2.

[57] Goswami R, Feng CR, Qadri SB, Pande CS. Fatigue-assisted grain growth in Al alloys. Nat Sci Rep 2017;7:10179. https://doi.org/10.1038/s41598-017-10889-8.

[58] Barcelo F, de Carlan Y, Béchade J-L, Fournier B. Orientation relationship in Eurofer martensitic steels. Phase Transit 2009;82:808–20. https://doi.org/10.1080/01411590903433242.

[59] Giordana MF, Alvarez-Armas I, Armas A. Microstructural characterization of EUROFER 97 during low-cycle fatigue. J Nucl Mater 2012;424:247–51. https://doi.org/10.1016/j.jnucmat.2012.03.019.

[60] Kuběna I, Polák J, Marmy P, Kruml T. A comparison of microstructure evolution due to fatigue loading in Eurofer 97 and ODS Eurofer steels. Procedia Eng 2014;74:401–4. https://doi.org/10.1016/j.proeng.2014.06.288.